Atmos. Meas. Tech. Discuss., doi:10.5194/amt-2017-47, 2017
Manuscript under review for journal Atmos. Meas. Tech.
Discussion started: 22 March 2017

Atmospheric Measurement Techniques Discussions

Aerosol type retrieval and uncertainty quantification from OMI data

Anu Kauppi[1,2], Pekka Kolmonen[1], Marko Laine[1], and Johanna Tamminen[1]

[1]Finnish Meteorological Institute, Helsinki, Finland
[2]Department of Mathematics and Statistics, University of Helsinki, Helsinki, Finland

Correspondence to: Anu Kauppi (anu.kauppi@fmi.fi)

Abstract.

We discuss uncertainty quantification for aerosol type selection in satellite-based atmospheric aerosol retrieval. The retrieval procedure uses pre-calculated aerosol microphysical models stored in look-up tables (LUTs) and top of atmosphere spectral reflectance measurements to solve the aerosol characteristics. The forward model approximations cause systematic differences between the modeled and observed reflectance. Acknowledging this model discrepancy as a source of uncertainty allows us to produce more realistic uncertainty estimates and assists the selection of the most appropriate LUTs for each individual retrieval.

This paper focuses on the aerosol microphysical model selection and characterization of uncertainty in the retrieved aerosol type and aerosol optical depth (AOD). The concept of model evidence is used as a tool for model comparison. The method is based on Bayesian inference approach where all uncertainties are described as a posterior probability distribution. When there is no single best matching aerosol microphysical model we use a statistical technique based on Bayesian model averaging to combine AOD posterior probability densities of the best fitting models to obtain an averaged AOD estimate. We also determine the shared evidence of the best matching models of a certain main aerosol type in order to quantify how plausible each main aerosol type is in representing the underlying atmospheric aerosol conditions.

The developed method is applied to Ozone Monitoring Instrument (OMI) measurements using multi-wavelength approach for retrieving the aerosol type and AOD estimate with uncertainty quantification for cloud-free over-land pixels. Several larger pixel set areas were studied in order to investigate robustness of the developed method. We evaluated the retrieved AOD by comparison with ground-based measurements at example sites. We found that the uncertainty of AOD expressed by posterior probability distribution reflects the difficulty in model selection. The posterior probability distribution can provide a comprehensive characterization of the uncertainty in this kind of problem for aerosol type selection. As a result, the proposed method can account for the model error and also include the model selection uncertainty in the total uncertainty budget.

1 Introduction

The atmospheric aerosols play an important role in our understanding of Earth's climate system. Aerosols have direct and indirect influence on Earth's radiation budget. Satellite remote sensing observations have been utilized for years to provide information about atmospheric aerosol conditions in global scale. The spaceborn data is very useful for detecting and following dynamic natural or anthropogenic events such as sand storms and active fires. The most common retrieved aerosol characteristic is the aerosol optical depth (AOD) which is a function of the loading, size distribution and optical properties of aerosol

Atmos. Meas. Tech. Discuss., doi:10.5194/amt-2017-47, 2017
Manuscript under review for journal Atmos. Meas. Tech.
Discussion started: 22 March 2017

Atmospheric Measurement Techniques Discussions

particles. There are a number of satellite instruments delivering aerosol products and providing aerosol characteristics e.g. the Ozone Monitoring Instrument (OMI) (Torres et al., 2007), the Moderate Resolution Imaging Spectroradiometer (MODIS) (Levy et al., 2010), the Global Ozone Monitoring Experiment-2 (GOME-2) (Hassinen et al., 2015), the Multi-angle Imaging SpectroRadiometer (MISR) (Kahn et al., 2010), the (Advanced) Along-Track Scanning Radiometers ((A)ATSR) (Thomas et al., 2009; Kolmonen et al., 2016), the Cloud-Aerosol Lidar and Infrared Path finder (CALIPSO) (Winker et al., 2009), the Scanning Imaging Absorption spectroMeter for Atmospheric Chartography (SCIAMACHY) (Bovensmann et al., 1999), the Polarisation and Directionality of the Earth's Reflectance (POLDER) (Dubovik et al., 2011) and the Spinning Enhanced Visible and Infrared Imager (SEVIRI) (Govaerts et al., 2010; Wagner et al., 2010).

There is an increasing potential for using and incorporating satellite-based aerosol information as the instruments are getting better in resolution and more sophisticated for detecting aerosols (Holzer-Popp et al., 2013). In addition, the improvement of retrieval algorithms and the development of novel methodologies extend opportunities to use the data. Especially, one target is to derive information about small aerosol particles (diameter less than 1 μm) from satellite measurements. An important and challenging use of satellite measurements is to assimilate aerosol characteristics into large-scale global aerosol models (Benedetti et al. , 2009). Furthermore, the satellite based data can be combined with numerical models when estimating aerosol emission fluxes (Huneeus et al., 2012). Data validness as well as identification and quantification of uncertainties are acknowledged when data is used.

Uncertainties in satellite-based aerosol retrievals arise from many sources, e.g. cloud contamination, treatment of surface reflectance and instrumental issues. It is typical in the aerosol retrievals that the radiative transfer (i.e. forward model) calculations have been replaced by pre-calculated look-up tables (LUTs) in order to speed up the needed computations. The LUTs are often multi-dimensional tables containing simulated discrete descriptions of varying aerosol conditions. Aerosols can be classified into categories (i.e. main types) such as clean background, urban pollution, dust, smoke (from biomass burning) and sea salt based on the origins of the aerosol particles. The optical and microphysical properties of different aerosol types are described in corresponding LUTs. The situation is more complicated for a retrieval algorithm when an aerosol containing air-mass is a mixture of different types, e.g. mixture of dust aerosols and biomass burning aerosols. The proper aerosol type selection from LUTs is a source of uncertainty and affects the accuracy of the retrieval. Povey et al. (2015) give an overview of the error analysis and representation of uncertainty in the satellite data. One application they discuss is related to the AOD retrievals where unquantifiable errors arise from the choice of a forward model (i.e. aerosol microphysical properties).

In this paper we discuss characterization of uncertainty in the aerosol type and AOD retrieval. We utilize the method, described in Määttä et al. (2014), for estimating the uncertainty in the retrieved AOD due to the aerosol microphysical model selection and the approximations in forward modeling. The method is based on the Bayesian inference approach where uncertainty estimates are an inherent part of the formulation (MacKay, 1992; Spiegelhalter et al., 2002; Robert, 2007). The uncertainty is given as a posterior density function of the AOD and a point estimate for the AOD is the maximum a posterior (MAP) value. We calculate the model evidence value for each aerosol microphysical model involved in order to compare models and do the model selection. The selection of single best fitting aerosol microphysical model is not always clear and this uncertainty has also been addressed in this study. We calculate the averaged posterior probability distribution where the

Atmos. Meas. Tech. Discuss., doi:10.5194/amt-2017-47, 2017
Manuscript under review for journal Atmos. Meas. Tech.
Discussion started: 22 March 2017

Atmospheric Measurement Techniques Discussions

individual model posterior distributions are weighted by their evidence. This is implemented by the Bayesian model averaging technique (Hoeting et al., 1999). We also perform the shared evidence of the best matching models within main aerosol type in order to quantify plausibility of each main aerosol type. We acknowledge the forward modeling uncertainty, i.e. model discrepancy (Kennedy et al., 2001; Brynjarsdóttir et al., 2014) which arises from non-modeled systematic differences between the modeled and observed reflectance. The described method is applied for the aerosol retrieval using cloud screened data from the OMI instrument.

The used data and methodology are introduced in Sect. 2 and 3. We have investigated the performance of the method with case studies presented in Sect. 4. Section 5 discuss the features and possibilities of the method.

2 OMI data

The Dutch-Finnish OMI instrument is on board NASA's Earth Observing System (EOS) Aura platform which was launched in July 2004 (Levelt et al., 2006). The Aura satellite is in a polar sun-synchronous orbit crossing the equator approximately at 13:45 local time. OMI measures sunlight backscattered from the Earth in the ultraviolet (UV) and visible (VIS) wavelength bands (270-500 nm). The ground pixel size at nadir is $13 \times 24\,\mathrm{km}^2$. The retrieved products include atmospheric trace gases (ozone, NO_2, SO_2, HCHO, BrO and OClO), surface UV, cloud information and aerosol characteristic.

The two operational aerosol algorithms to retrieve aerosol characteristics from OMI measurements are the OMI near-UV aerosol data product (OMAERUV) and the OMI multi-wavelength aerosol data product (OMAERO) (Torres et al., 2007, 2002). OMAERUV uses in the retrieval two wavelength bands at 354 and 388 nm to determine the AOD, aerosol index and single scattering albedo (Ahn et al., 2014). OMAERO uses the near UV and visible wavelengths between 330 and 500 nm providing the AOD, best matching aerosol model and aerosol characteristics associated with the best model (e.g. single scattering albedo and aerosol indices) (Curier et al., 2008). The retrievals of AOD and single scattering albedo from OMAERUV and OMAERO have been evaluated using air-borne sunphotometer, ground-based sun/sky radiometer and other satellite measurements (Ahn et al., 2008; Livingston et al., 2009).

The OMI data used in this study have been extracted via Mirador data search tool provided by the NASA Goddard Earth Sciences Data and Information Services Center (GES DISC) data access system (https://urs.earthdata.nasa.gov). We calculated the top-of-the-atmosphere (TOA) spectral reflectance (referred as measured or observed reflectance from now on) from the OMI Level 1B VIS and UV radiances and Level 1B Solar irradiance data. We took the effective cloud fraction information from the Level 2 OMI O_2-O_2 cloud product (OMCLDO2). Then we applied a simple scheme by using 0.34 as an effective cloud fraction threshold value for detecting and excluding a cloudy ground pixel. Thus we followed only one of three tests for cloud screening used by the OMAERO algorithm. The high threshold value of 0.34 was chosen in order to avoid excluding desert dust scenes (OMAERO Readme Document, 2011). To assure measurement data quality in the retrieval we used the pixel wise quality and error flags from the OMI Level 1B radiance products. In addition, to ensure the forward model quality, we excluded data where solar zenith angle was above 75°.

Atmos. Meas. Tech. Discuss., doi:10.5194/amt-2017-47, 2017
Manuscript under review for journal Atmos. Meas. Tech.
Discussion started: 22 March 2017

Atmospheric Measurement Techniques Discussions

We used GroundPixelQuality flag from the OMI Level 1B radiance product to choose the over land pixels as this study was concentrated on the aerosol types that are dominant over land areas. We accepted a pixel and specify it as land pixel if the flag indicated ground type to be land, shallow inland water, ocean coastline/lake shoreline, ephemeral (intermittent) water or deep inland water (OMI Level 1B Output products and Metadata, 2009). We used the climatological surface reflectance database from the OMI Earth Surface Reflectance Climatology product OMLER (v003). The OMLER (v003) product data file (OMI-Aura_L3-OMLER_2005m01-2009m12_v003-2010m0503t063707.he5) was extracted from the GES DISC data Service. The OMLER product contains in a 0.5 x 0.5 degree grid global maps of the monthly climatology of Lambert equivalent reflectance (LER) based on five years (2005-2009) of OMI data (OMLER Readme Document, 2010).

In our analysis we have used about 1 nm wide wavelength bands centered at 342.5, 367.0, 376.5, 388.0, 399.5, 406.0, 416.0, 425.5, 436.5, 442.0, 451.5, 463.0 and 483.5 nm. These 13 bands include one wavelength in the UV region and the rest in the VIS region. We note that we have omitted in our study the O2-O2 absorption wavelength band centered at 477 nm. The band 477 nm brings important information about the cloud height and for cloud-free scene about the aerosol layer height for high enough AOD levels (Veihelmann et al., 2007).

2.1 Aerosol microphysical models

The aerosol microphysical models stored in the OMI LUTs are produced via the radiative transfer calculations for a range of aerosol physical properties and sun-satellite geometries (Torres et al., 2002, 2007). There are four main aerosol types: weakly absorbing (WA), biomass burning (BB), desert dust (DD) and volcanic (VO) aerosols. The weakly absorbing type aerosol models are composed of urban-industrial and natural oceanic aerosols (Torres et al., 2002). Veihelmann et al. (2007) discuss the capability of the OMI multi-wavelength algorithm to distinguish between different aerosol types.

The main types are split into sub-types (i.e. models) according to the aerosol size distribution, refractive index and vertical profile. We used a set of OMI aerosol microphysical models, total of fifty models, in the work presented here (see Table 1). Each model consists of a set of parameters (e.g. AOD, single scattering albedo, viewing and solar zenith angle, relative azimuth angle, path reflectance, transmission and spherical albedo) with predefined values at node points.

A weakly absorbing aerosol model 'WA1114' represents sea salt particles having a higher fraction of coarse particles than the other weakly absorbing models (see Table 1). We have classified the model 'WA1114' as the fifth main aerosol type when reporting results from the case examples (see Sect. 4).

3 Methodology

The proposed method is applied to the retrieval scheme that is similar to the OMAERO algorithm. The unknown aerosol parameter is the AOD at the reference wavelength of 500 nm, for which we will use symbol τ. The related uncertainty is analyzed using Bayesian statistical inference. The observations are TOA reflectances $\boldsymbol{R}_{\mathrm{obs}}(\lambda)$ at a set of wavelengths $\lambda = (\lambda_1, \ldots, \lambda_n)$. The modeled spectral reflectance $\boldsymbol{R}_{\mathrm{mod}}(\tau, \lambda)$ depends on τ within the specific aerosol microphysical model in

Atmos. Meas. Tech. Discuss., doi:10.5194/amt-2017-47, 2017
Manuscript under review for journal Atmos. Meas. Tech.
Discussion started: 22 March 2017

Atmospheric Measurement Techniques Discussions

LUT. The AOD parameter τ is adjusted between the nodal values in the model LUT to find the modeled reflectance that has the best fit with the observed spectral reflectance.

The formula for the modeled reflectance above a Lambertian surface over a land pixel is

$$\boldsymbol{R}_{\text{mod}}(\lambda, \tau, \mu, \mu_0, \Delta\phi, p_{\text{s}}) = R_a(\lambda, \tau, \mu, \mu_0, \Delta\phi, p_{\text{s}}) + \frac{A_{\text{s}}(\lambda)}{1 - A_{\text{s}}(\lambda)\, s(\lambda, \tau, p_{\text{s}})} T(\lambda, \tau, \mu, \mu_0, p_{\text{s}}). \quad (1)$$

In the formula, path reflectance R_a, transmittance T and spherical albedo s of the atmosphere are derived by LUT interpolation as a function of λ, τ, $\Delta\phi$ (relative azimuth angle), p_{s} (surface pressure), μ (cosine of viewing zenith angle) and μ_0 (cosine of solar zenith angle). The surface reflectance A_{s} is taken from the Lambertian equivalent surface reflectance climatology based on the geolocation of the retrieved pixel and month.

3.1 Acknowledging the model discrepancy

The aerosol microphysical models used in the retrieval procedure are discrete representations of the real atmosphere. This forward model approximation error, together with uncertainties in the assumptions, e.g. in the surface reflectance, cause model discrepancy, which manifests itself as systematic deviations between the modeled and observed reflectance.

In general description of a retrieval method, a measurement noise term includes the measurement and forward model error. We pay special attention to the model discrepancy in the fitting process by adding the related uncertainty term $\eta(\lambda)$ to the observation model

$$\boldsymbol{R}_{\text{obs}}(\lambda) = \boldsymbol{R}_{\text{mod}}(\tau, \lambda) + \eta(\lambda) + \epsilon_{\text{obs}}(\lambda). \quad (2)$$

The new model discrepancy error term $\eta(\lambda)$ enables correlated errors between neighboring wavelengths, thus allowing for smooth departures from the model. The measurement error term $\epsilon_{\text{obs}}(\lambda)$ will describe the independent instrument noise that will be assumed to be known in the retrieval procedure coming from the instrument properties and from the calculation of the observed reflectance. In the fitting procedure, for simplicity, we use measurement error $\epsilon_{\text{obs}}(\lambda)$ determined as $\boldsymbol{R}_{\text{obs}}(\lambda)$/SNR, where SNR = 500 is the signal-to-noise ratio of the instrument.

Our approach to estimate the model discrepancy term $\eta(\lambda)$ was to explore systematic differences between the measured and modeled reflectance (i.e. residuals). The systematic structure in the residuals indicates inadequacy in the forward model. The model discrepancy was characterized using a zero mean Gaussian process $\eta(\lambda) \sim GP(0, \mathbf{C})$ (Rasmussen and Williams, 2006) as described by Määttä et al. (2014). The covariance function $\mathbf{C}$ of the Gaussian process defines the correlation properties of the discrepancy. We constructed the covariance function empirically by using the wavelength distance dependent correlation structure of the residuals (see Määttä et al. (2014) for details).

As a result, the likelihood function has an additional error covariance term due to the model error,

$$p(\boldsymbol{R}_{\text{obs}}|\tau, m) \propto \exp\left(-\frac{1}{2}\boldsymbol{R}_{\text{res}}(\lambda)^T \left(\mathbf{C} + \text{diag}\left(\sigma^2(\lambda)\right)\right)^{-1} \boldsymbol{R}_{\text{res}}(\lambda)\right), \quad (3)$$

where $\boldsymbol{R}_{\text{res}}(\lambda) = \boldsymbol{R}_{\text{obs}}(\lambda) - \boldsymbol{R}_{\text{mod}}(\tau, \lambda)$ is the residual, $\mathbf{C}$ is the model discrepancy covariance matrix and $\text{diag}(\sigma^2(\lambda))$ is a diagonal matrix of the measurement error variances $\sigma^2(\lambda)$. The likelihood function is needed for calculation of posterior distribution using Bayes' formula (see Sect. 3.2).

Atmos. Meas. Tech. Discuss., doi:10.5194/amt-2017-47, 2017
Manuscript under review for journal Atmos. Meas. Tech.
Discussion started: 22 March 2017

Atmospheric Measurement Techniques Discussions

3.2 Aerosol type and AOD retrieval with uncertainty quantification

In the Bayesian inference, the solution of an inverse problem is presented as a posterior distribution of the unknown. This approach provides a natural way to present the uncertainty in the AOD and in the aerosol microphysical model m. By Bayes' formula the posterior distribution for τ within the model m and given the observed reflectance $\boldsymbol{R}_{\text{obs}}$ is

$$p(\tau|\boldsymbol{R}_{\text{obs}}, m) = \frac{p(\boldsymbol{R}_{\text{obs}}|\tau, m)\, p(\tau|m)}{p(\boldsymbol{R}_{\text{obs}}|m)}, \tag{4}$$

where $p(\boldsymbol{R}_{\text{obs}}|\tau, m)$ is the likelihood and $p(\tau|m)$ is a prior distribution for τ depending on the aerosol microphysical model m. The denominator $p(\boldsymbol{R}_{\text{obs}}|m)$ does not depend on τ and acts to normalize the numerator. The calculation of the actual posterior distribution requires solving integrals over the parameter and model space. In the present case, the estimation and model selection procedure seeks the solution for a one-dimensional parameter τ, and the calculations will be fairly straightforward by numerical quadrature. The posterior distribution calculation is presented in more detail in Määttä et al. (2014).

The denominator $p(\boldsymbol{R}_{\text{obs}}|m)$ in Eq. (4) is the probability of the observed reflectance $\boldsymbol{R}_{\text{obs}}$ assuming the model m is the correct one. However, when considering our problem of choosing the right model m, the $p(\boldsymbol{R}_{\text{obs}}|m)$ acts as an evidence in favour for m. Consequently, we compare models using their evidence values. In the retrieval procedure we accept the models with the highest evidence until a cumulative sum of the selected models' evidences pass the value of 0.8 or the number of selected models is ten.

Since we assume that a priori all models are equally likely, we end up calculating the relative evidence for each selected model m_i by formula

$$p(m_i|\boldsymbol{R}_{\text{obs}}) = \frac{p(\boldsymbol{R}_{\text{obs}}|m_i)}{\sum_j p(\boldsymbol{R}_{\text{obs}}|m_j)}. \tag{5}$$

Here the denominator is a sum over all the evidences of the models m_j under the comparison process (see Määttä et al. (2014) for details). The relative evidence indicates how plausible the aerosol microphysical model is among the set of potential models.

Even when a model has the highest evidence it does not ensure that it gives an adequate fit to the observed reflectance. The goodness of fit of the selected model is analyzed by the modified chi-squared value

$$\chi^2 = \frac{1}{n-1} \boldsymbol{R}_{\text{res}}(\lambda)^{\text{T}} \left(\mathbf{C} + \text{diag}(\sigma^2(\lambda))\right)^{-1} \boldsymbol{R}_{\text{res}}(\lambda), \tag{6}$$

where $\mathbf{C}$ is a covariance matrix for the model discrepancy and n is the number of wavelength bands in the spectral reflectance. We accepted the retrieved solution (i.e. the selected best model) if this merit function gives a value ≤ 2.

3.3 Bayesian model averaging

Traditionally, the aerosol microphysical model m_i with the highest evidence can be treated as the correct one. However, there can be several models that could explain the measurements equally well when taking into account the uncertainty in the selection procedure. In that case the selection of single model (i.e. aerosol sub-type) does not ensure that it is the most appropriate model since it may have been selected by chance. In addition, the posterior distribution for τ can differ from model

Atmos. Meas. Tech. Discuss., doi:10.5194/amt-2017-47, 2017
Manuscript under review for journal Atmos. Meas. Tech.
Discussion started: 22 March 2017

Atmospheric Measurement Techniques Discussions

to model among the best models. This indicates that the selection of one particular model as the correct one is not always self-evident or meaningful.

We have used the Bayesian model averaging approach (Hoeting et al., 1999; Robert, 2007) to calculate averaged posterior distribution by formula

$$p_{\text{avg}}(\tau|\boldsymbol{R}_{\text{obs}}) = \sum_{i=1}^{n} p(\tau|\boldsymbol{R}_{\text{obs}}, m_i)\, p(m_i|\boldsymbol{R}_{\text{obs}}), \tag{7}$$

where the posterior distributions for τ, assuming that m_i is the correct model, are weighted by the models' evidences. By model averaging we perform the shared inference about the AOD over the best fitting models. Secondly, the uncertainty in the model selection is incorporated in the uncertainty estimate of the AOD.

4 Case studies and results

With the following test cases we study functioning of the aerosol type selection procedure, concept of the evidence for model comparison and the resulted AOD posterior distribution for expressing the uncertainty due to model selection and approximations in forward modeling. The relative evidence of a single model, with respect to the other selected models, describes the plausibility of that model to explain the observed reflectance. The width of the posterior density function illustrates the level of the uncertainty, i.e. the wider the width the higher the uncertainty.

We consider two test cases where the atmospheric aerosol conditions are different from each other. The first case study focuses on an urban area around Beijing, where we analyze the retrieved aerosol characteristics on two days to observe the difference as well as similarity of aerosol conditions in these days. The Beijing case is challenging since the aerosol air-mass is a mixture of dust from north blending with urban pollution around Beijing. On the other hand, this case enables to examine aerosol type selection in situation with high AOD levels. The other test case cover Northern and Central Africa where we expect dust aerosols in the north and biomass burning aerosols in the central part. In particular, this test case cover large, almost cloud free, area.

We evaluated the retrieved AOD estimates using collocated ground-based Aerosol Robotic Network (AERONET) data of aerosol properties. The AERONET program is a federation of ground-based remote sensing aerosol networks (Holben et al., 1998). We downloaded the Version 2 Direct sun Level 2.0 quality assured and cloud-screened aerosol data for the AERONET sites under investigation.

4.1 Beijing area on 16 April and 27 April 2008

In this case study focusing on an urban area around Beijing, we analyzed the retrieved aerosol characteristics on two days: the 16th and 27th of April 2008. In the spring season the atmosphere is typically loaded by a mixture of urban and dust aerosols (Yu et al., 2016). Figure 1 shows the true-colour images from the MODIS, on-board the NASA's Aqua satellite, on the 16th of April 2008 at 05:15 UTC (left) and 27th of April 2008 at 04:55 UTC (right) over the Beijing area.

Atmos. Meas. Tech. Discuss., doi:10.5194/amt-2017-47, 2017
Manuscript under review for journal Atmos. Meas. Tech.
Discussion started: 22 March 2017

Atmospheric Measurement Techniques Discussions

The OMI pixels are located on rows 23-29 across the orbit in the first day case (i.e. the 16th of April) and on rows 10-20 in the second day case (i.e. the 27th of April), respectively. The pixel has no data if it is cloud contaminated or none of the models had adequate fit with the measured reflectance (Eq. 6).

Figure 2 presents the number of most appropriate models retrieved for each pixel on both days. The maximum number of best models was restricted to ten (see Sect. 3.2). In the first day case the variety of the number of best models is wide (left) whereas in the latter day case (right) for the most part of the pixels the maximum number of models are selected to explain the measurements.

In Fig. 3 is shown the distribution of the main aerosol types of the retrieved aerosol microphysical models (i.e. sub-types) having the highest evidence. The main aerosol types are the weakly absorbing (WA), weakly absorbing sea salt (WA1114), biomass burning (BB), desert dust (DD) and volcanic (VO) aerosols. The prevailing types in both days in the vicinity of Beijing AERONET site (marked with black star in Fig. 3) are the BB and WA types. The appearance of marine type 'WA1114' as the best matching type may occur due to cloud impact since the nearby pixels with no results have been omitted as cloudy pixels. In addition, on the 27th of April (right) the desert dust type gets the highest evidence in the upper part of the examination area. An airmass trajectory analysis (not shown here) indicated that on the 27th dust from the Gobi desert (north of the study area) was entering the Beijing area.

Figures 4 and 5 illustrate for both days how plausible each main aerosol type is to represent the prevailing aerosol air-mass type. We have summed up the relative evidences (%) of the selected models (i.e. sub-types) within each main type to get a quantity of confidence, i.e. shared evidence, for each main aerosol type. Figures b-f show pixel wise the shared evidence (%) for each main type. Whereas, the figure on the upper left corner (a) presents the relative evidence (%) of the single best fitting aerosol microphysical model indicating how superior the ranked best model is with respect to the other selected models if any. We can notice that the one best model does not necessarily determine the aerosol type alone, but a mixture of models could give a better match. We also observe that both WA and BB type aerosol microphysical models get support as representative models for some pixel areas (b-d). In addition, in the latter day case the DD type gets strong evidence in the upper right corner of the examination area (Fig. 5e).

Figure 6 shows the distribution of the retrieved MAP AOD estimates in both days. The upper row show the MAP estimate from the aerosol microphysical model with the highest evidence. The lower row show the MAP estimate from the averaged posterior distribution over the selected best models. In general, the AOD point estimate value from the averaged posterior distribution is lower than the AOD estimate based on the single best model.

Figure 7 shows the results for a single pixel having a geometric collocation with the AERONET Beijing site, i.e. the Beijing site coordinates are inside an OMI pixel. The upper row shows the measured reflectance (in blue) and the selected, best matching, modeled reflectances (in green) for the 16th of April (left) and the 27th of April (right). In the lower row are shown the posterior density functions that characterize the uncertainty. Also, the best matching models' identification numbers and the associated relative evidences inside brackets are given. The relative evidence (%) (Eq. 5) express how plausible this model is to explain the measured spectral reflectance with respect to the other selected best models. The averaged posterior distribution (Eq. 7) has two peaks indicating difficulty in model selection. The red vertical dashed line denotes the MAP AOD estimate

(i.e. the posterior mode) from the averaged posterior. The grey vertical lines show the AERONET AOD at 500 nm values at separate measurement times.

On the 16th of April (left) there are two best matching models, both of the BB type, selected. The width of the averaged posterior is relatively wide indicating high uncertainty in the result. The model with the higher evidence has much weight in the averaged posterior and this affects the retrieved AOD that is higher than the AERONET values. The AERONET measurements are in the time range of 00:02-04:59 UTC therefore before the OMI overflight time ($\sim$ 5:25 UTC). However, there are some AERONET AOD measurements (n=3) within two hours time window including OMI overpass time. These AOD values are marked by darker grey vertical lines and the black vertical line is the average. Figure 8 shows the best fitted modeled reflectances when we considered only weakly absorbing type models' LUTs. We can see that the match with the observed reflectance is not as good as the selected best BB models have (Fig. 7 left).

On the 27th of April (Fig. 7 right) we can be confident with the result as it is in agreement with the AERONET data. There is one WA type model (blue posterior curve) ranked as the second best model in the fitting. At that time the AERONET measurement are in time range of 08:22-09:43 UTC, thus monitored after the OMI overpass time ($\sim$ 5:06 UTC).

In Table 2 are given the aerosol characteristics for the AERONET sites and results, e.g. AOD at 500 nm and Ångström exponent values, retrieved by the proposed method. The AERONET data for Beijing shown in Table 2 are the daily averages. We interpolated AOD at 500 nm by using the AERONET AOD at 440 nm and the AERONET provided Ångström exponent 440-675 nm. The Ångström exponent describes the dependency of the AOD on wavelength. It gives an approximation of the aerosol particle size in such a way that when coarse aerosol particles dominate the exponent is small, and vice versa for the fine particle dominance. In our retrieval we calculated the Ångström exponent (442-500 nm) by Ångström exponent power law where the AOD at 442 nm was derived from the associated LUT based on the retrieved AOD at 500 nm. Thus the reported Ångström exponent is completely determined by the model LUT. In Table 2 are presented Ångström exponent values based on the best fitted ($\alpha 1$) and the second best fitted ($\alpha 2$) model.

4.2 Northern and Central Africa on 26 March 2008

This case study covers a large area over the Northern and Central Africa on the 26th of March 2008. Figure 9 shows the MODIS true-colour images on the 26th of March 2008 at 13:00 and at 13:05 UTC over the Northern and Central Africa. The view is mainly cloud free except for some broken-cloud cover in coastal regions. The AOD data from four AERONET sites Agoufou (North Mali), DMN_Maine_Soroa (Niger), IER_Cinzana (Mali) and Saada (Morocco) are used to evaluate the results. Daily averaged AERONET Version 2 Direct sun Level 2.0 AOD data are reported in Table 2.

In Fig. 10 we can see the areas where the maximum number of aerosol microphysical models are selected, as well as the areas where only one model dominates. In the middle of the orbit is an area where none of the models has adequate fit with the measured reflectance (Eq. 6). In March 2008 the rows 54-55 (i.e. 53-54 if 0-based) in the OMI measurements are affected by a row anomaly (OMI row anomaly team, 2016). We have omitted these two rows in the analysis.

As seen in Fig. 11 the desert dust is the dominating type of the selected best models. There are also areas where the BB type of models get the highest evidence to explain the measurement. The pixels where the weakly absorbing sea salt type aerosols

(type WA1114) have the best fit are located in the edge areas of clouds or in partly cloudy areas (see Fig. 9). The unexpected volcanic aerosol type appears as the only best aerosol type in the pixels located northeast from the Lake Chad. The selection of volcanic type is most probably related to a white area seen in the MODIS RGB Fig. 9 (left). The location of AERONET sites are marked with black stars.

The Figs. 12b-f reveal that all the selected best models (i.e. sub-types) usually are of the same main type, namely BB or DD type. But, in the area around Algeria occurrence of a mixture of main types may be related to the cloud contamination of these pixels.

From the Fig. 13 it can be concluded that often the MAP estimate from the single best aerosol microphysical model has slightly higher AOD level (left) than the MAP estimate from the averaged posterior distribution over the selected best models (right). The retrieved AOD estimates are rather small perhaps indicating that no dust event or active fires were going on. However, we can notice that in the area south of the latitude of 8°, where the biomass burning type of models dominate, the AOD estimates are higher. Active fire maps from satellite data (not shown here) support the fire activity at that area. We can also notice the DD type dominating area near the Agoufou AERONET site where AOD level is higher (see Fig. 13 and Fig. 12e).

Figure 14 shows the Ångström exponent (442-500 nm) values based on the best fitted (left) and the second best fitted (right) model. In the Table 2 are shown the calculated Ångström exponent (442-500 nm) values at the locations of the reference AERONET sites. Again, it should be noted here that the retrieved Ångström exponent is completely determined by the model LUT. Consequently, as seen in Fig. 14 the Ångström parameters reflect the selected aerosol microphysical models.

Figures 15 and 16 show the spectral reflectance fitting curves (on the left hand side) and the retrieved AOD estimates with uncertainty (on the right hand side) for the single pixels located around the AERONET sites: Agoufou, DMN_Maine_Soroa, IER_Cinzana and Saada. In the figure showing the posterior distributions (right) the grey vertical lines indicate AERONET Direct sun Level 2.0 AOD at 500 nm values measured during that day. The darker grey vertical lines denote AERONET AOD values within two hour time window including the OMI overpass time and the black vertical line is the average of these AOD values.

The measured reflectance at the Agoufou site (first row in Fig. 15) has a rather unique spectral structure but there is one dust type model that fits to the measured reflectance adequately well. The associated AOD from the model LUT is unreasonable high with respect to AERONET values. Also the large width of posterior indicates high uncertainty. It can be noted here that AERONET measurements at the Agoufou site were made in the morning in time range of 06:58-09:27 UTC whereas the OMI overpass time at that location was at $\sim$ 13:15 UTC.

At the other three reference AERONET sites there are measured AOD values during the OMI overpass time. In Fig. 15, showing the results for DMN_Maine_Soroa case (lower row), all the ten selected models belong to the biomass burning type and their posteriors indicate an uniform small uncertainty. The estimated AOD values are consistent with the AERONET AOD values within uncertainty. In the IER_Cinzana case (Fig. 16 upper row) the selected models are the desert dust type (orange) except for one biomass burning type model (red curve). The estimated AOD is a bit lower than the AERONET measurements. In the Saada case (Fig. 16 bottom row) the AERONET AOD values are in good agreement with estimated AOD, although the

averaged AERONET AOD (black vertical line) of measurements around the OMI overpass time is slightly lower than the MAP estimate of AOD (red dashed vertical line).

5 Discussion and Conclusions

In this paper, we focused on the aerosol microphysical model selection in the aerosol retrieval and on the quantification of uncertainty for the retrieved aerosol type and AOD using OMI TOA spectral reflectance measurements. The retrieval scheme is similar to the OMAERO algorithm using information from several wavelength bands between 330 and 500 nm and pre-calculated LUTs for aerosol microphysical properties. The presented methodology was previously used by Määttä et al. (2014) for the retrieval of AOD at the reference wavelength of 500 nm. This new research investigates the uncertainty in the aerosol type selection in more detail. For simplicity, we studied only cloud-free over-land OMI pixels.

The method uses Bayesian statistical inference to quantify uncertainties due to model selection and due to approximations in the forward modeling. The concept of model evidence is used as a tool for model comparison and to assist in the selection of the best models. The forward model approximations cause model error that results in systematic differences between the modeled and observed reflectance. We acknowledge this model discrepancy when choosing the most appropriate LUTs in order to produce more realistic uncertainty estimates of the retrieved AOD. Following the Bayesian approach the uncertainty is described by the posterior probability distribution. The selection of single best fitting aerosol microphysical model is not always clear and this uncertainty is addressed in this study. We use a statistical technique based on Bayesian model averaging to combine the AOD posterior probability densities of the best models to obtain the averaged posterior distribution. Then the retrieved AOD is the MAP estimate of the averaged posterior function. We also determine the shared evidence of the best matching models within a main aerosol type (weakly absorbing, sea salt, biomass burning, dust and volcanic) in order to quantify plausibility of each main aerosol type.

Retrieving the aerosol type and AOD from the TOA reflectance measurements is an ill-posed problem and a priori information of prevailing aerosol conditions are needed to get a solution. The limited information content in the OMI measurements and the narrow wavelength band range ending up to 500 nm make the problem very challenging to solve. We investigated the developed method by studies covering several larger pixel set areas. We evaluated the retrieved AOD by comparison with AERONET measurements at example sites.

In our approach we did not pre-select aerosol microphysical models based on e.g. a climatology of aerosol geographical distribution. Instead, we fitted all the available models (i.e. LUTs) to the spectral measurement. This makes the whole process slower but is justified here to study the uncertainty in the aerosol model selection. The goodness-of-fit value (Eq. 6) was used to analyze whether the retrieved solution is acceptable. We used a limited set of aerosol microphysical models, a total of fifty models. It is highly likely that the used model set is not comprehensive enough to represent all aerosol air-mass conditions. In the Beijing case studies the absorbing biomass burning type aerosol microphysical models dominate (Sect. 4.1) and the reason could be the lack of proper models for the prevailing aerosol conditions during the selected days. In addition, in the Northern

and Central Africa case (Sect. 4.2) there is an area in the middle of the orbit where none of the available models gave an adequate fit.

We made the cloud screening in a straightforward way just using the effective cloud fraction threshold value of 0.34 (see Sect. 2) and thus there were most probably cloud affected pixels left. The suspicious results were often localized to pixels in the edge of a cloud or inside broken-cloud areas. In these cases the observed reflectance was such that the unexpected model, e.g. an oceanic or volcanic aerosol model, had the best fit. This feature could be used as an additional cloud detection.

Here the model discrepancy was determined empirically by exploring a set of residuals (i.e. the difference between observed and modeled reflectance) and then fitting a Gaussian process to find the characteristics of the model error (see Määttä et al., 2014). Brynjarsdóttir et al. (2014) discussed model discrepancy and its effect on results with simple examples. They also emphasized the importance of modeling the model error properly and the use of realistic priors for the model discrepancy.

The aerosol type selection from LUTs is a source of uncertainty and affects the accuracy of the retrieval. The aim of our study was to produce more realistic uncertainty estimates. As a result, we can account for the model error and also include the model selection uncertainty in the total uncertainty budget. The case studies indicate that the developed methodology works in the varying aerosol conditions as expected. We found that the increased uncertainty of AOD expressed by the posterior distribution reflects the difficulty in model selection. The posterior probability distribution can characterize the uncertainty more extensively than commonly given standard deviation.

The method described in this work is applicable to any instrument measurements where the observed reflectance is available as well as the aerosol microphysical models. Our plan is to apply this method to an AATSR retrieval algorithm where the models are constructed during the fitting using a limited amount of aerosol components describing non-absorbing and absorbing fine particles together with coarse marine and dust particles (Kolmonen et al., 2016).

Acknowledgements. This work was supported by the Academy of Finland INQUIRE project and by the European Space Agency as part of the Aerosol_cci project. The OMI data was extracted via the NASA's GES DISC Mirador data access system. The authors like to thank the OMI Science Team for providing the data. The authors would like to give many thanks to the KNMI OMI team for providing the aerosol model look-up tables (LUTs) used in this study and discussions on the OMAERO algorithm. The authors also thank the Principal Investigators and their staff for establishing and maintaining Beijing, Agoufou, DMN_Maine_Soroa, IER_Cinzana and Saada AERONET sites.

References

Ahn, C., Torres, O., and Bhartia, P. K.: Comparison of ozone monitoring instrument UV aerosol products with Aqua/Moderate Resolution Imaging Spectroradiometer and Multiangle Imaging Spectroradiometer observations in 2006, J. Geophys. Res. Atmos., 113, D16S27, doi::10.1029/2007JD008832, 2008.

Ahn, C., Torres, O., and Jethva, H.: Assessment of OMI near-UV aerosol optical depth over land, J. Geophys. Res. Atmos., 119, 2457–2473, doi:10.1002/2013JD020188, 2014.

Benedetti, A., Morcrette, J.-J., Boucher, O., Dethof, A., Engelen, R. J., Fisher, M., Flentje, H., Huneeus, N., Jones, L., Kaiser, J. W., Kinne, S., Mangold, A., Razinger, M., Simmons, A. J., and Suttie, M.: Aerosol analysis and forecast in the European Centre for Medium-Range Weather Forecasts Integrated Forecast System: 2. Data assimilation, J. Geophys. Res., 114, D13205, doi:10.1029/2008JD011115, 2009.

Bovensmann, H., Burrows, J., Buchwitz, M., Frerick, J., Noël, S., Rozanov, V., Chance, K., and Goede, A,: SCIAMACHY: Mission objectives and measurement modes, J. Atmos. Sci., 56, 127–150, 1999.

Brynjarsdóttir, J., and O'Hagan, A.: Learning about physical parameters: the importance of model discrepancy, Inverse problems, 30, 2014.

Curier, R. L., Veefkind, J. P., Braak, R., Veihelmann, B., Torres, O., and de Leeuw, G.: Retrieval of aerosol optical properties from OMI radiances using a multiwavelength algorithm: Application to western Europe, J. Geophys. Res., 113, D17S90, doi:10.1029/2007JD008738, 2008.

Dubovik, O., Herman, M., Holdak, A., Lapyonok, T., Tanré, D., Deuzé, J. L., Ducos, F., Sinyuk, A., and Lopatin, A.: Statistically optimized inversion algorithm for enhanced retrieval of aerosol properties from spectral multi-angle polarimetric satellite observations, Atmos. Meas. Tech., 4, 975–1018, doi:10.5194/amt-4-975-2011, 2011.

Gelman, A., Carlin, J. B., Stern, H. S., Dunson, D., Vehtari, A., and Rubin, D. B.: Bayesian Data Analysis, 3rd Edn., Chapman & Hall/CRC, 2013.

Govaerts, Y. M., Wagner, S., Lattanzio, A., and Watts, P.: Joint retrieval of surface reflectance and aerosol optical depth from MSG/SEVIRI observations with an optimal estimation approach: 1. Theory, J. Geophys. Res., 115, D02203, doi:10.1029/2009JD011779, 2010.

Hassinen, S., Balis, D., Bauer, H., Begoin, M., Delcloo, A., Eleftheratos, K., Gimeno Garcia, S., Granville, J., Grossi, M., Hao, N., Hedelt, P., Hendrick, F., Hess, M., Heue, K.-P., Hovila, J., Jønch-Sørensen, H., Kalakoski, N., Kauppi, A., Kiemle, S., Kins, L., Koukouli, M. E., Kujanpää, J., Lambert, J.-C., Lang, R., Lerot, C., Loyola, D., Pedergnana, M., Pinardi, G., Romahn, F., van Roozendael, M., Lutz, R., De Smedt, I., Stammes, P., Steinbrecht, W., Tamminen, J., Theys, N., Tilstra, L. G., Tuinder, O. N. E., Valks, P., Zerefos, C., Zimmer, W., and Zyrichidou, I.: Overview of the O3M SAF GOME-2 operational atmospheric composition and UV radiation data products and data availability, Atmos. Meas. Tech., 9, 383–407, doi:10.5194/amt-9-383-2016, 2016.

Hoeting, J. A., Madigan, D., Raftery, A. E., and Volinsky, C. T.: Bayesian Model averaging: A Tutorial, Statist. Sci., 14, 382–417, 1999.

Holben, B. N., Eck, T. F., Slutsker, I., Tanré, D., Buis, J. P., Setzer, A., Vermote, E., Reagan, J. A., Kaufman, Y. J., Nakajima, T., Lavenu, F., Jankowiak, I., and Smirnov, A.: AERONET – a federated instrument network and data archive for aerosol characterization, Remote Sens. Environ., 66, 1–16, 1998.

Holzer-Popp, T., de Leeuw, G., Griesfeller, J., Martynenko, D., Klüser, L., Bevan, S., Davies, W., Ducos, F., Deuzé, J. L.. Graigner, R. G., Heckel, A., von Hoyningen-Hüne, W., Kolmonen, P., Litvinov, P., North, P., Poulsen, C. A., Ramon, D., Siddans, R., Sogacheva, L., Tanre, D., Thomas, G. E., Vountas, M., Descloitres, J., Griesfeller, J., Kinne, S., Schulz, M. and Pinnock, S.: Aerosol retrieval experiments in the ESA Aerosol_cci project, Atmos. Meas. Tech., 6, 1919–1957, doi:10.5194/amt-6-1919-2013, 2013.

Huneeus, N., Chevallier, F., and Boucher, O.: Estimating aerosol emissions by assimilating observed aerosol optical depth in a global aerosol model, Atmos. Chem. Phys., 12, 4585–4606, doi:10.5194/acp-12-4585-2012, 2012.

Kahn, R. A., Gaitley, B. J., Garay, M. J., Diner, D. J., Eck, T. F., Smirnov, A., and Holben, B. N.: Multiangle Imaging Spectro-Radiometer global aerosol product assessment by comparison with the Aerosol Robotic Network, J. Geophys. Res., 115, D23209, doi:10.1029/2010JD014601, 2010.

Kennedy, M. C. and O'Hagan, A.: Bayesian Calibration of Computer Models, J. Roy. Stat. Soc. B, 63, 425–464, 2001.

Kolmonen, P., Sogacheva, L., Virtanen, T.H., de Leeuw, G., and Kulmala, M.: The ADV/ASV AATSR aerosol retrieval algorithm: current status and presentation of a full-mission AOD data set, Int. J. Digital Earth, 9, 545–561, 2016.

Levelt, P. F., van den Oord, G. H. J., Dobber, M. R., Mälkki, A., Visser, H., de Vries, J., Stammes, P., Lundell, J. O. V., and Saari, H.: The Ozone Monitoring Instrument, IEEE T. Geosci. Remote, 44, 1093–1101, 2006.

Levy, R. C., Remer, L. A., Kleidman, R. G., Mattoo, S., Ichoku, C., Kahn, R., and Eck, T. F.: Global evaluation of the Collection 5 MODIS dark-target aerosol products over land, Atmos. Chem. Phys., 10, 10399–10420, doi:10.5194/acp-10-10399-2010, 2010.

Livingston, J. M., Redemann, J., Russell, P. B., Torres, O., Veihelmann, B., Veefkind, P., Braak, R., Smirnov, A., Remer, L., Bergstrom, R. W., Coddington, O., Schmidt, K. S., Pilewskie, P., Johnson, R., and Zhang, Q.: Comparison of aerosol optical depths from the Ozone Monitoring Instrument (OMI) on Aura with results from airborne sunphotometry, other space and ground measurements during MILAGRO/INTEX-B, Atmos. Chem. Phys., 9, 6743-6765, 2009.

MacKay, D. J. C.: Bayesian interpolation, Neural Comput., 4, 415–447, doi:10.1162/neco.1992.4.3.415, 1991.

Määttä, A., Laine, M., Tamminen, J., and Veefkind, J. P.: Quantification of uncertainty in aerosol optical thickness retrieval arising from aerosol microphysical model and other sources, applied to Ozone Monitoring Instrument (OMI) measurements, Atmos. Meas. Tech., 7, 1185–1199, doi:10.5194/amt-7-1185-2014, 2014.

OMAERO Readme Document: OMAERO README file, available at: https://disc.sci.gsfc.nasa.gov/Aura/data-holdings/OMI/documents/v003/OMAERO_README_V003.doc/view (last access: 17 March 2017), 2011.

OMI Level 1B Output products and Metadata, available at: https://disc.gsfc.nasa.gov/Aura/data-holdings/OMI/documents/v003/RD01_SD467_IODS_Vol_2_issue8.pdf (last access: 29 December 2016), 2009.

OMI row anomaly team: Background information about the Row Anomaly in OMI, available at: http://projects.knmi.nl/omi/research/product/rowanomaly-background.php (last access: 29 December 2016).

OMLER Readme Document: OMI Surface Reflectance Climatology README, available at: https://projects.knmi.nl/omi/research/product/reflectance/OMI-Aura_L3-OMLER_2005m01-2009m12_v003-README.pdf (last access: 29 December 2016), 2010.

Povey, A. C., and Grainger, R. G.: Known and unknown unknowns: uncertainty estimation in satellite remote sensing, Atmos. Meas. Tech., 8, 4699–4718, doi:10.5194/amt-8-4699-2015, 2015.

Rasmussen, C. E. and Williams, C. K. I.: Gaussian Processes for Machine Learning, available at: http://www.GaussianProcess.org/gpml (last access: 29 December 2016), The MITT Press, 2006.

Robert, C. P.: The Bayesian Choice, From Decision-Theoretic Foundations to Computational Implementation, 2nd Edn., Springer, New York, 2007.

Spiegelhalter, D. J., Best, N. G., Carlin, B. P., and van der Linde, A.: Bayesian measures of model complexity and fit, J. Roy. Stat. Soc. B, 64, 583–639, 2002.

Thomas, G. E., Poulsen, C. A., Sayer, A. M., Marsh, S. H., Dean, S. M., Carboni, E., Siddans, R., Grainger, R. G., and Lawrence, B. N.: The GRAPE aerosol retrieval algorithm, Atmos. Meas. Tech., 2, 679–701, doi:10.5194/amt-2-679-2009, 2009.

Atmos. Meas. Tech. Discuss., doi:10.5194/amt-2017-47, 2017
Manuscript under review for journal Atmos. Meas. Tech.
Discussion started: 22 March 2017

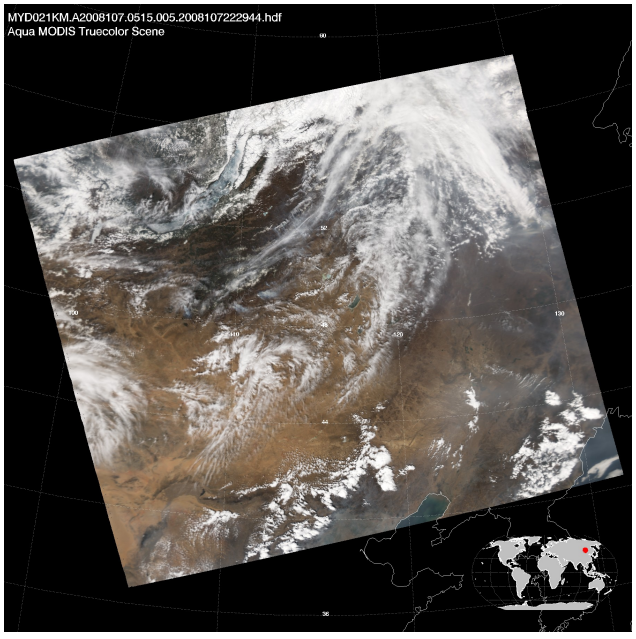

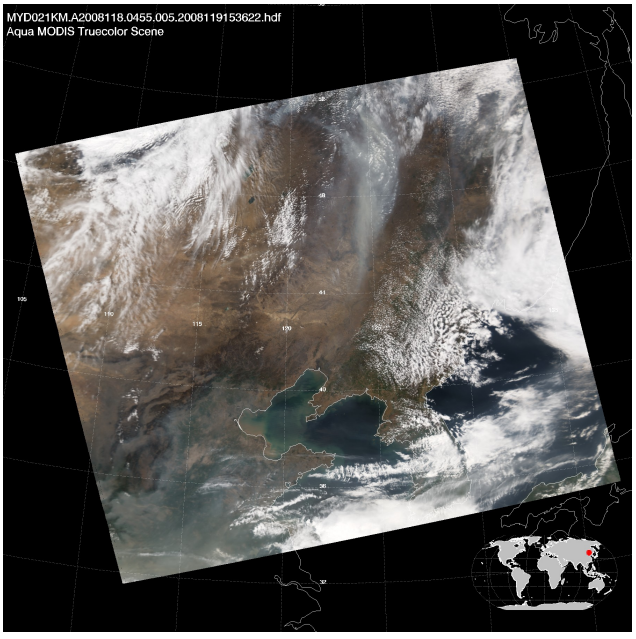

Figure 1. True-colour MODIS image (RGB) on 16 April 2008 at 05:15 UTC (left) and on 27 April 2008 at 04:55 UTC (right) over Beijing area. MODIS, on Aqua satellite, has the equator crossing time only about 15 minutes earlier than OMI.

Torres, O., Decae, R., Veefkind, J. P., and de Leeuw, G.: OMI Aerosol Retrieval Algorithm, in: OMI Algorithm Theoretical Basis Document: Clouds, Aerosols, and Surface UV Irradiance, 3, version 2, OMI-ATBD-03, edited by: Stammes, P., NASA Goddard Space Flight Center, Greenbelt, Md, 47–71, 2002.

Torres, O., Tanskanen, A., Veihelmann, B., Ahn, C., Braak, R., Bhartia, P. K., Veefkind, P., and Levelt, P.: Aerosols and surface UV products from Ozone Monitoring Instrument observations: An overwiew, J. Geophys. Res., 112, D24S47, doi:10.1029/2007JD008809, 2007.

Veihelmann, B., Levelt, P. F., Stammes, P., and Veefkind, J. P.: Simulation study of the aerosol information content in OMI spectral reflectance measurements, Atmos. Chem. Phys., 7, 3115–3127, doi:10.5194/acp-7-3115-2007, 2007.

Wagner, S. C., Govaerts, Y. M., and Lattanzio, A.: Joint retrieval of surface reflectance and aerosol optical depth from MSG/SEVIRI observations with an optimal estimation approach: 2. Implementation and evaluation, J. Geophys. Res., 115, D02204, doi:10.1029/2009JD011780, 2010.

Winker, D. M.,Vaughan, M. A., Omar, A. H., Hu, Y., Powell, K. A., Liu, Z., Hunt, W. H., and Young, S. A.: Overview of the CALIPSO mission and CALIOP data processing algorithms, J. Atmos. Ocean. Tech., 26, 2310–2323, doi:10.1175/2009JTECHA1281.1, 2009.

Yu, X., Lü, R, Kumar, K. R., Ma J., Zhang, Q., Jiang, Y., Kang, N., Yang, S., Wang, J., and Li, M.: Dust aerosol properties and radiative forcing observed in spring during 2001–2014 over urban Beijing, China, Environ. Sci. Pollut. Res., 23, 15432–15442, doi:10.1007/s11356-016-6729-9, 2016.

Atmos. Meas. Tech. Discuss., doi:10.5194/amt-2017-47, 2017
Manuscript under review for journal Atmos. Meas. Tech.
Discussion started: 22 March 2017

Atmospheric Measurement Techniques Discussions

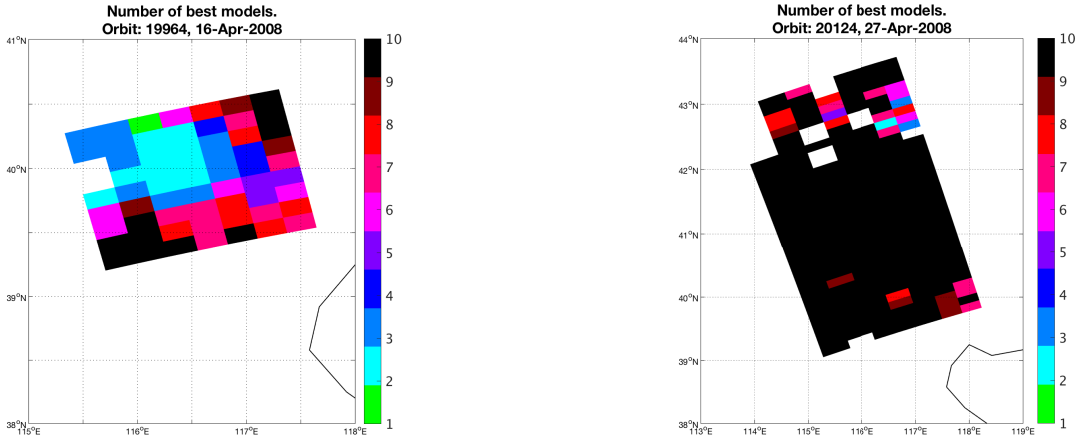

Figure 2. The number of most appropriate aerosol microphysical models at the retrieved pixels on 16th April (left) and 27th April (right).

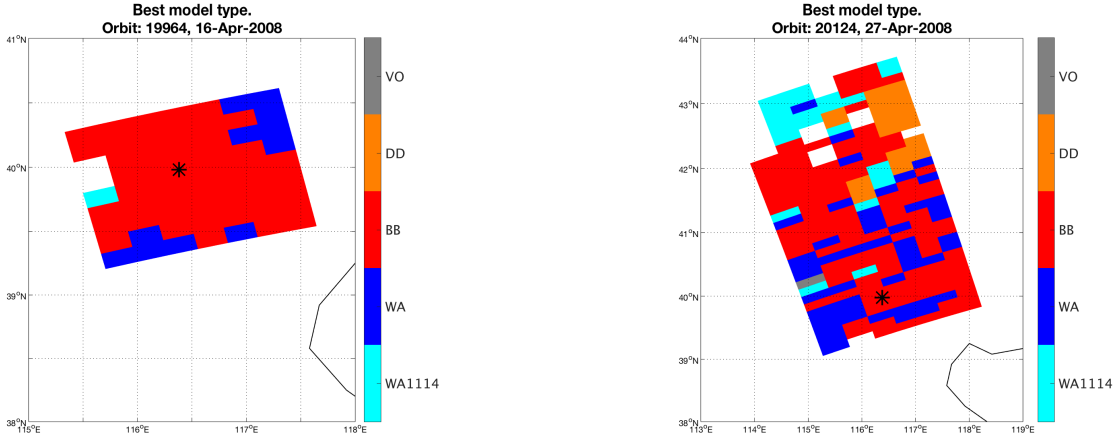

Figure 3. The main aerosol type of the retrieved model with the highest evidence i.e. the best model, on 16th April (left) and 27th April (right). The main aerosol types are: WA1114 (Weakly absorbing sea salt), WA (Weakly absorbing), BB (Biomass burning), DD (Desert dust) and VO (Volcanic). The location of AERONET site Beijing, China, (see Table 2) is marked by a black star.

Atmos. Meas. Tech. Discuss., doi:10.5194/amt-2017-47, 2017
Manuscript under review for journal Atmos. Meas. Tech.
Discussion started: 22 March 2017

Atmospheric Measurement Techniques Discussions

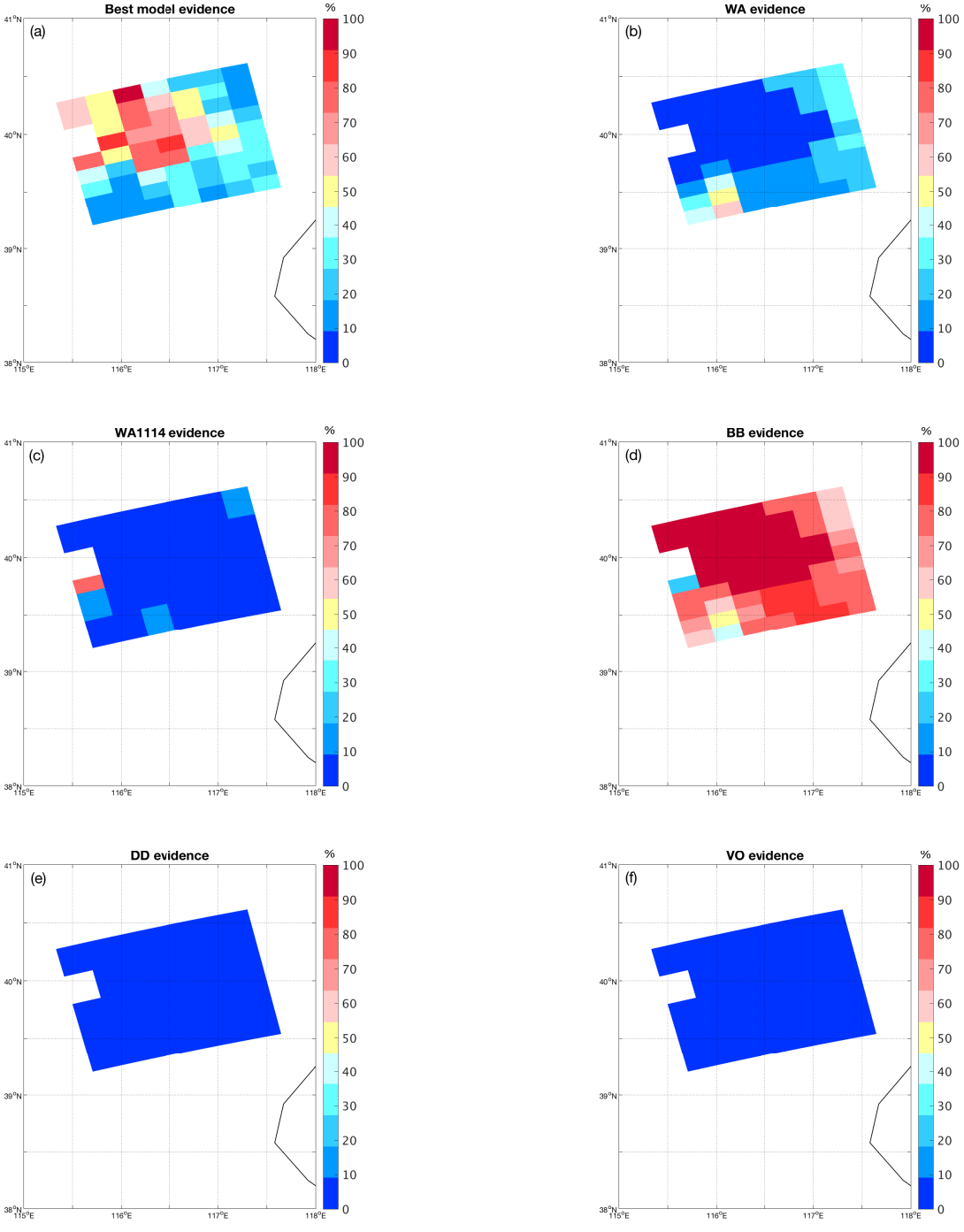

Figure 4. The relative evidence distribution (%) of the selected models on 16th April 2008. (a) The relative evidence of the best model with the highest evidence and the shared evidence of the best models of each main aerosol type: (b) weakly absorbing, (c) weakly absorbing sea salt, (d) biomass burning, (e) desert dust and (f) volcanic aerosols.

Atmos. Meas. Tech. Discuss., doi:10.5194/amt-2017-47, 2017
Manuscript under review for journal Atmos. Meas. Tech.
Discussion started: 22 March 2017

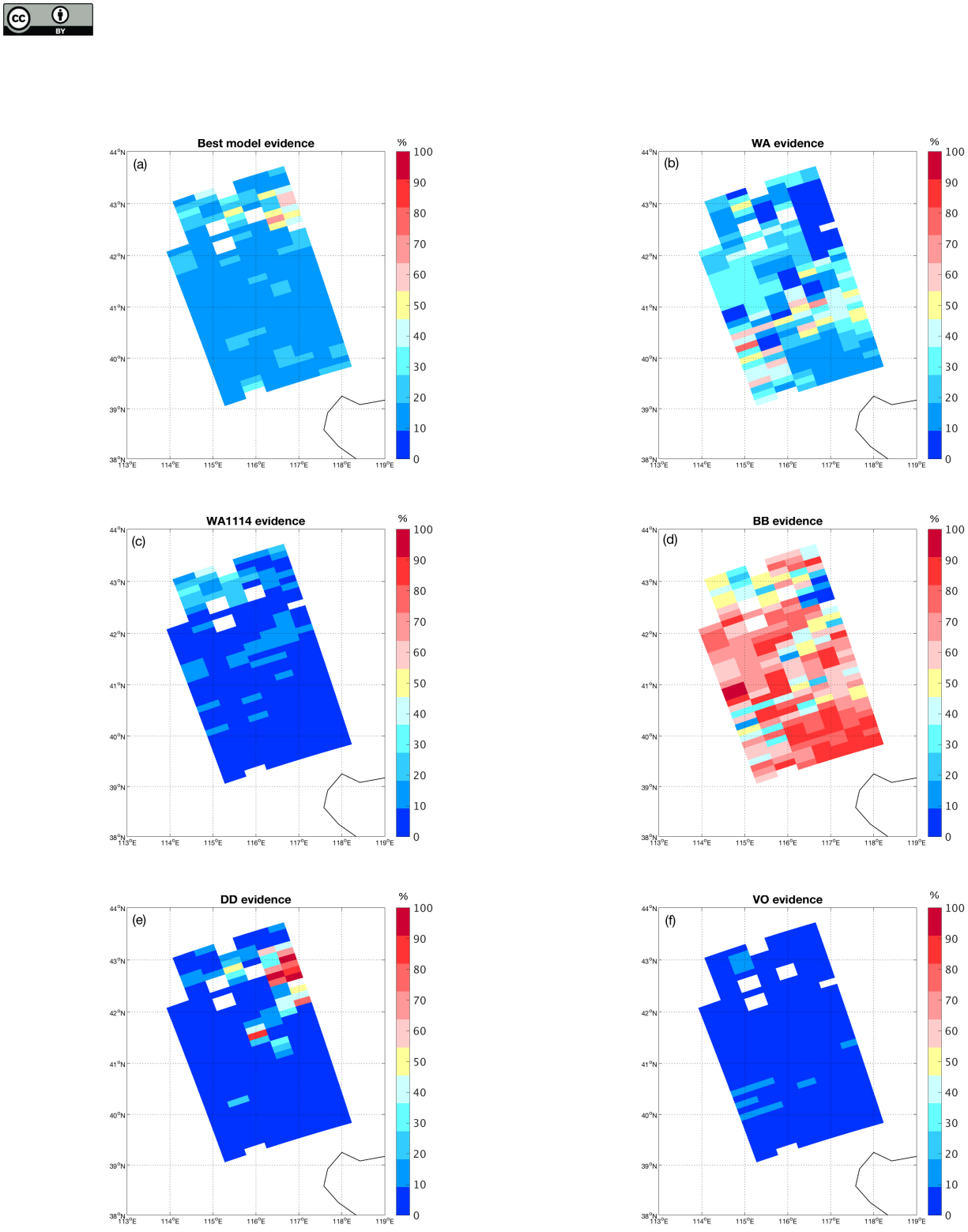

Figure 5. Same as Fig. 4 but the relative evidence distribution (%) of the selected best models on 27th April 2008.

Atmos. Meas. Tech. Discuss., doi:10.5194/amt-2017-47, 2017
Manuscript under review for journal Atmos. Meas. Tech.
Discussion started: 22 March 2017

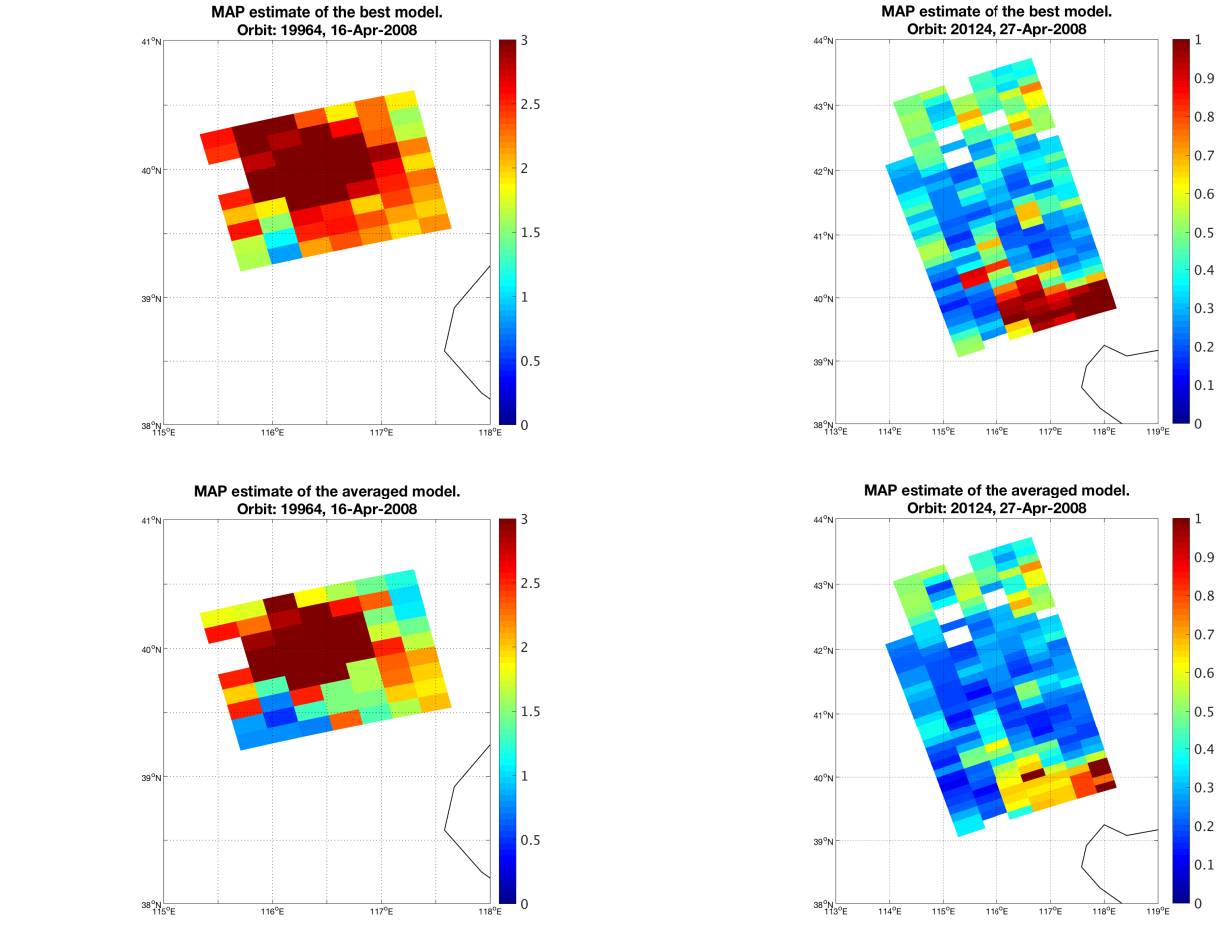

Figure 6. The MAP estimate of AOD based on the best model (upper row) and based on the averaged posterior distribution (lower row) shown for 16th April (left) and 27th April (right). Please note the different colour scale.

Atmos. Meas. Tech. Discuss., doi:10.5194/amt-2017-47, 2017
Manuscript under review for journal Atmos. Meas. Tech.
Discussion started: 22 March 2017

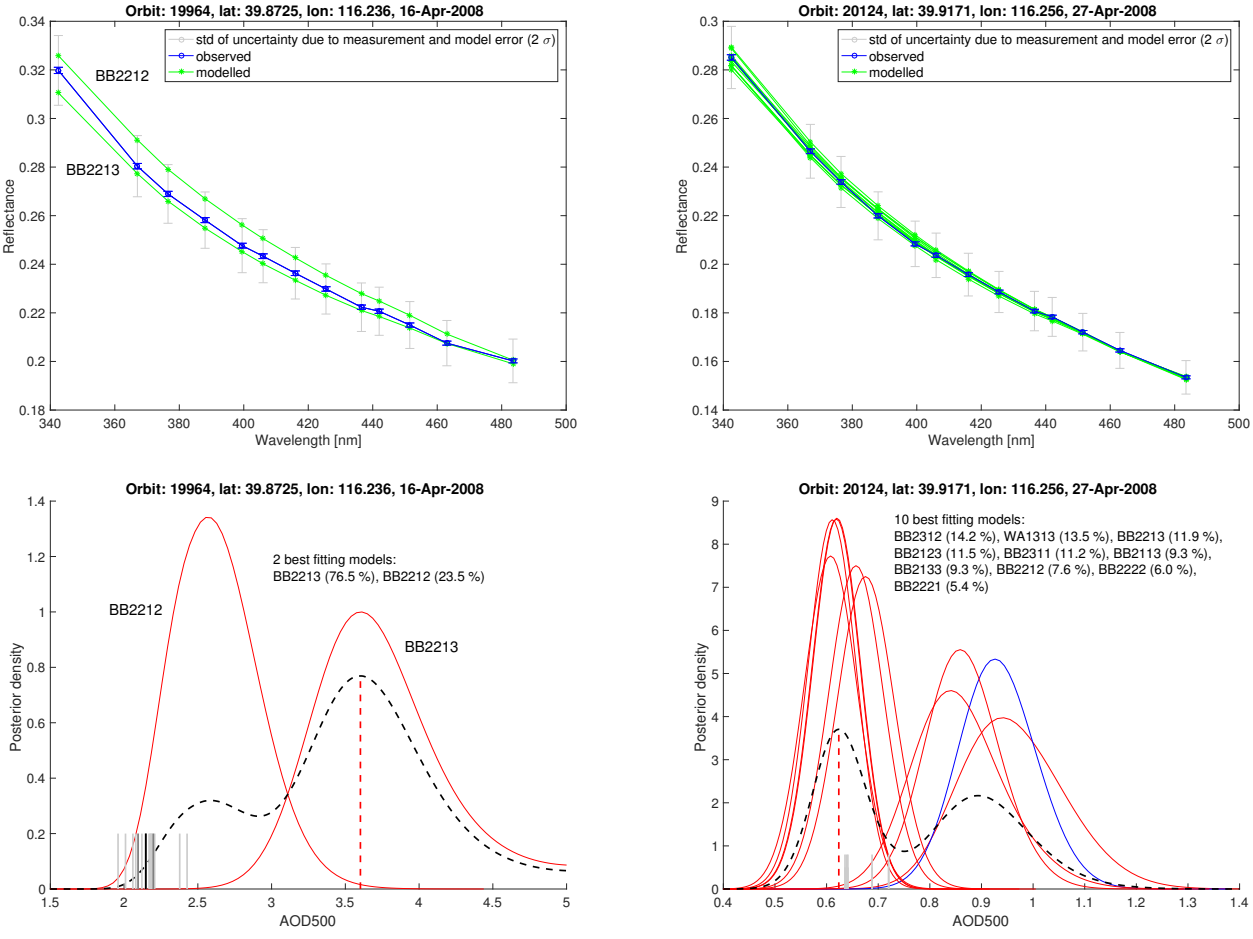

Figure 7. Beijing, 16th April (on the left) and 27th April (on the right). Upper row: The observed reflectance (blue dots) and modeled reflectance (green dots) of the selected best fitting models. The error-bars in blue correspond to 2 x standard measurement error and the error-bars in grey correspond to 2 x standard uncertainty due to measurement and model error. Lower row: The posterior probability distribution of AOD for each best fitting model. The biomass burning type model's posterior density curve is in red and weakly absorbing type model's curve in blue. The dashed black curve is the averaged posterior distribution over the best fitting models (Eq. 7). The red vertical dashed line indicates the MAP estimate from the averaged posterior distribution. The grey vertical lines show AERONET Version 2 Direct sun Level 2 AOD at 500 nm values position at the horizontal axis. The darker grey vertical lines (bottom left hand panel) denote AERONET AOD values (n=3) within two hours time window including OMI overpass time and the black vertical line is the average of these values.

Atmos. Meas. Tech. Discuss., doi:10.5194/amt-2017-47, 2017
Manuscript under review for journal Atmos. Meas. Tech.
Discussion started: 22 March 2017

Atmospheric Measurement Techniques Discussions

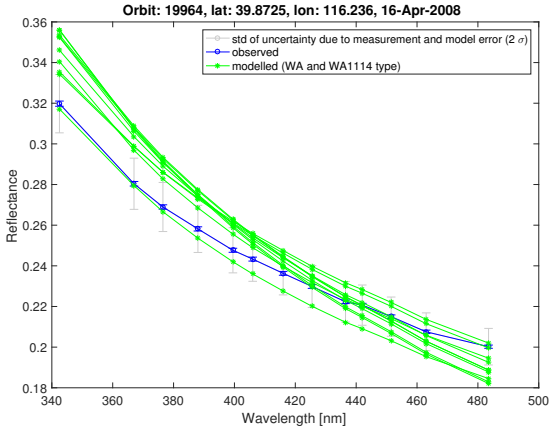

Figure 8. Beijing, 16 April. The modeled reflectances from weakly absorbing and marine WA1114 type models' LUTs are fitted to the observed reflectance.

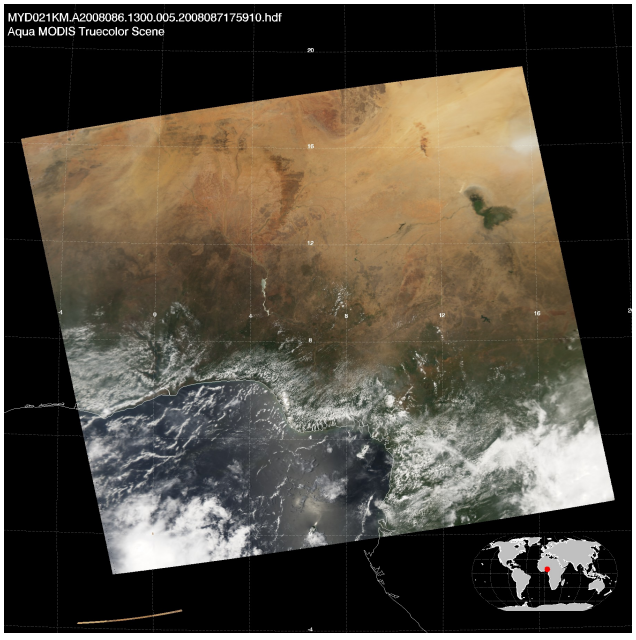

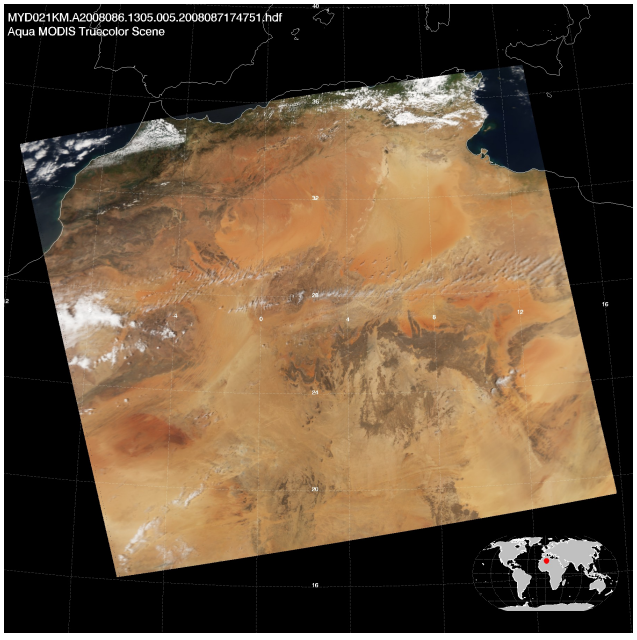

Figure 9. True-colour MODIS image (RGB) on 26 March 2008 at 13:00 UTC (left) and 13:05 UTC (right).

Atmos. Meas. Tech. Discuss., doi:10.5194/amt-2017-47, 2017
Manuscript under review for journal Atmos. Meas. Tech.
Discussion started: 22 March 2017

Atmospheric Measurement Techniques Discussions

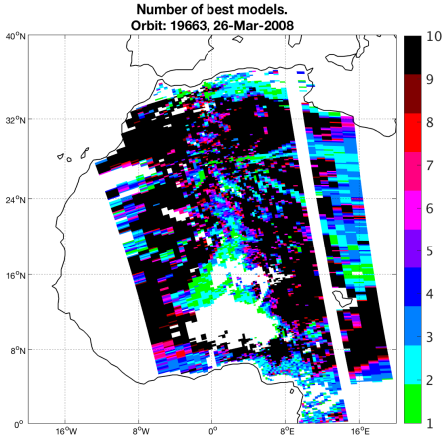

Figure 10. The number of most appropriate aerosol microphysical models at the retrieved pixels.

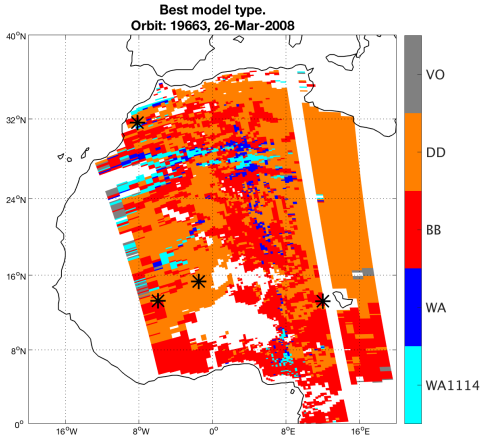

Figure 11. The main aerosol type of the retrieved model model with the highest evidence. The locations of AERONET sites Agoufou, DMN_Maine_Soroa, IER_Cinzana and Saada (see Table 2) are marked by black stars.

Atmos. Meas. Tech. Discuss., doi:10.5194/amt-2017-47, 2017
Manuscript under review for journal Atmos. Meas. Tech.
Discussion started: 22 March 2017

Atmospheric Measurement Techniques Discussions

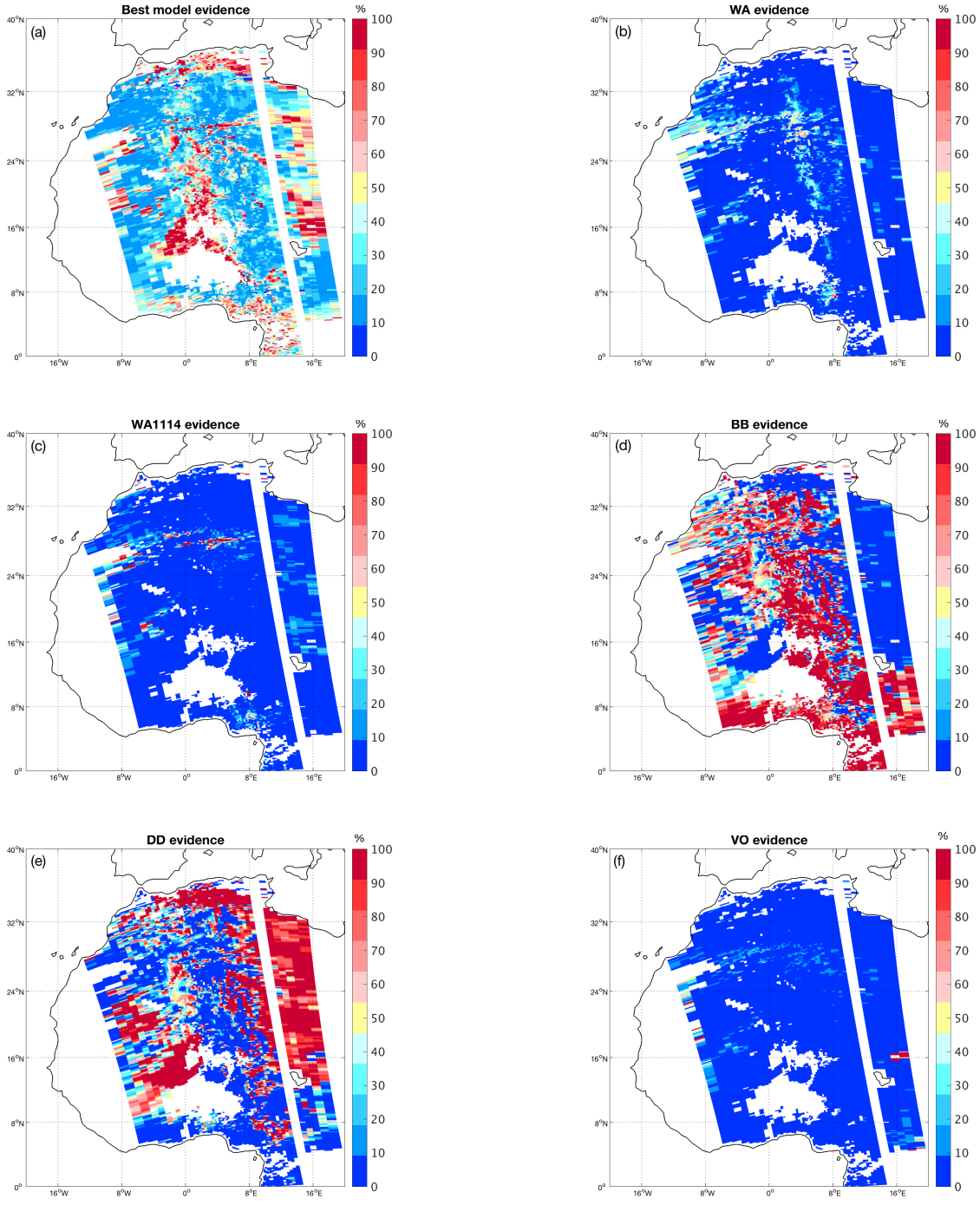

Figure 12. Same as Fig. 4 but the relative evidence distribution (%) of the selected best models in Africa case on 26th March 2008.

Atmos. Meas. Tech. Discuss., doi:10.5194/amt-2017-47, 2017
Manuscript under review for journal Atmos. Meas. Tech.
Discussion started: 22 March 2017

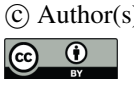

Atmospheric Measurement Techniques Discussions

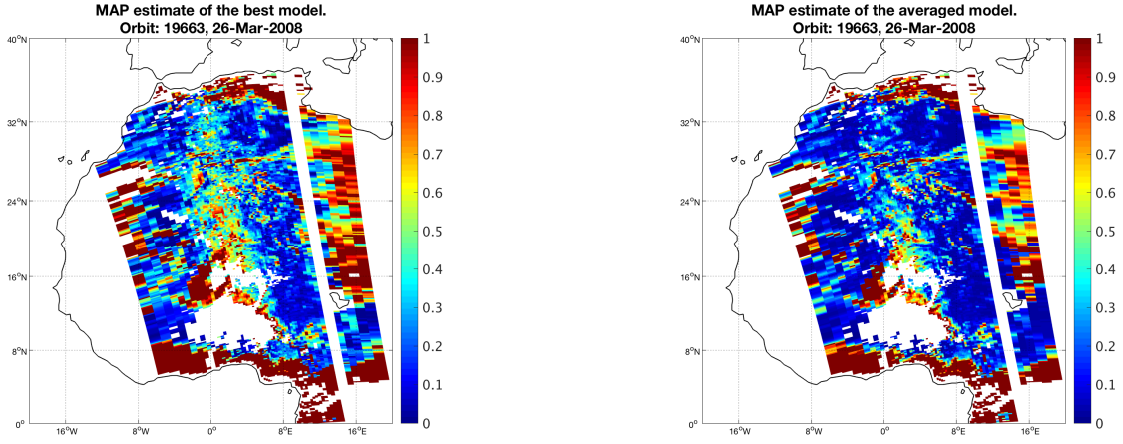

Figure 13. The MAP estimate for AOD based on the best model (left) and based on the averaged posterior distribution (right).

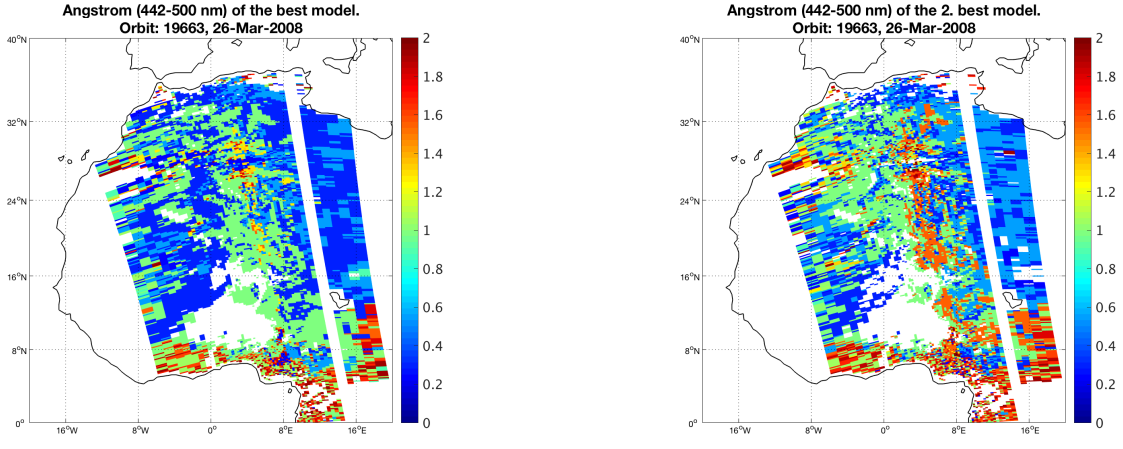

Figure 14. The Ångström exponent at 442-500 nm of the ranked best (left) and the second best (right) aerosol microphysical model.

Atmos. Meas. Tech. Discuss., doi:10.5194/amt-2017-47, 2017
Manuscript under review for journal Atmos. Meas. Tech.
Discussion started: 22 March 2017

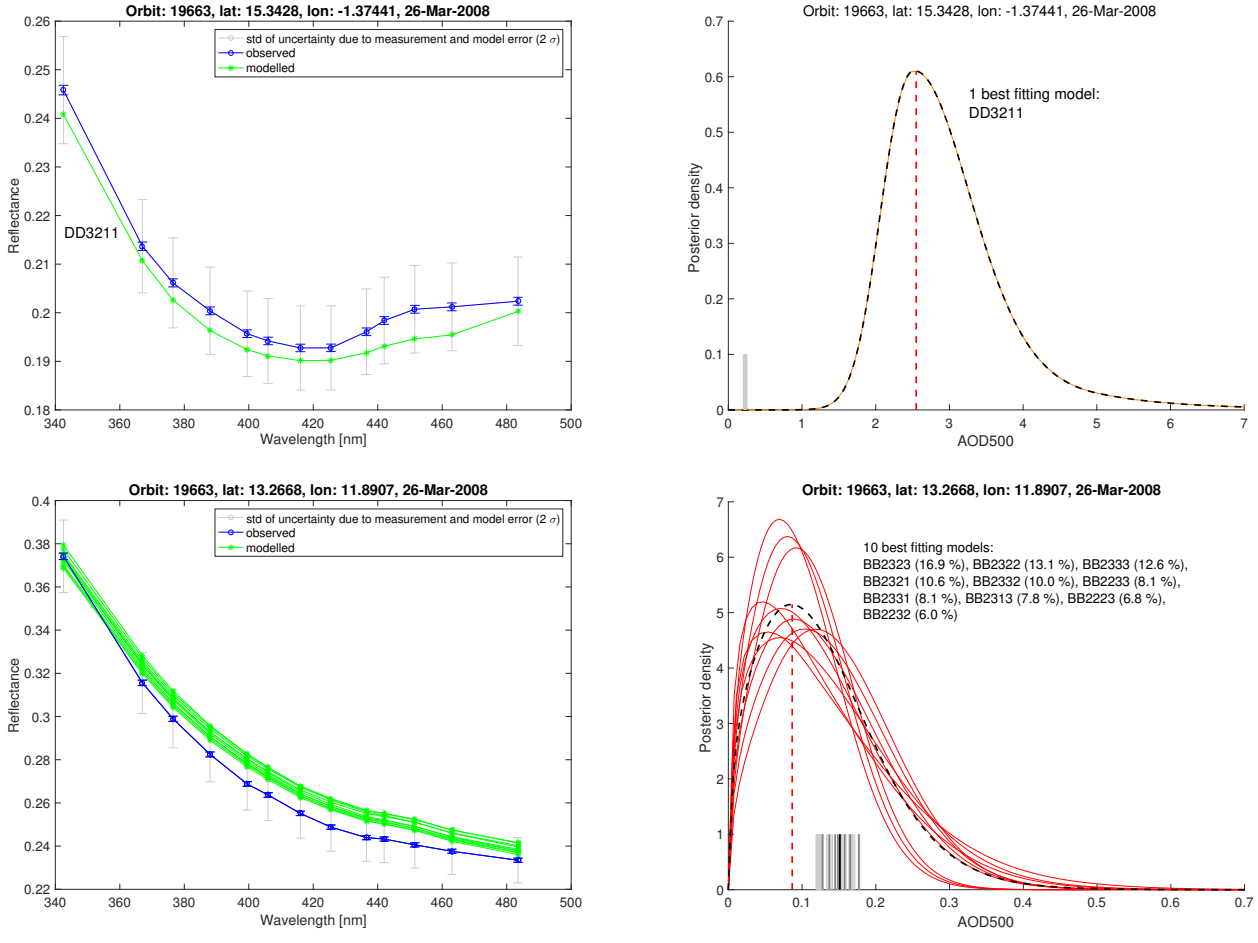

Figure 15. Same as Fig. 7 but for the pixels located at Agoufou (upper row) and DMN_Maine_Soroa (lower row). The grey vertical lines show AERONET Version 2 Direct sun Level 2 AOD at 500 nm values. The darker grey vertical lines (bottom right hand panel) denote AERONET AOD values within two hours time window including OMI overpass time and the black vertical line is the average of these values.

Atmos. Meas. Tech. Discuss., doi:10.5194/amt-2017-47, 2017
Manuscript under review for journal Atmos. Meas. Tech.
Discussion started: 22 March 2017

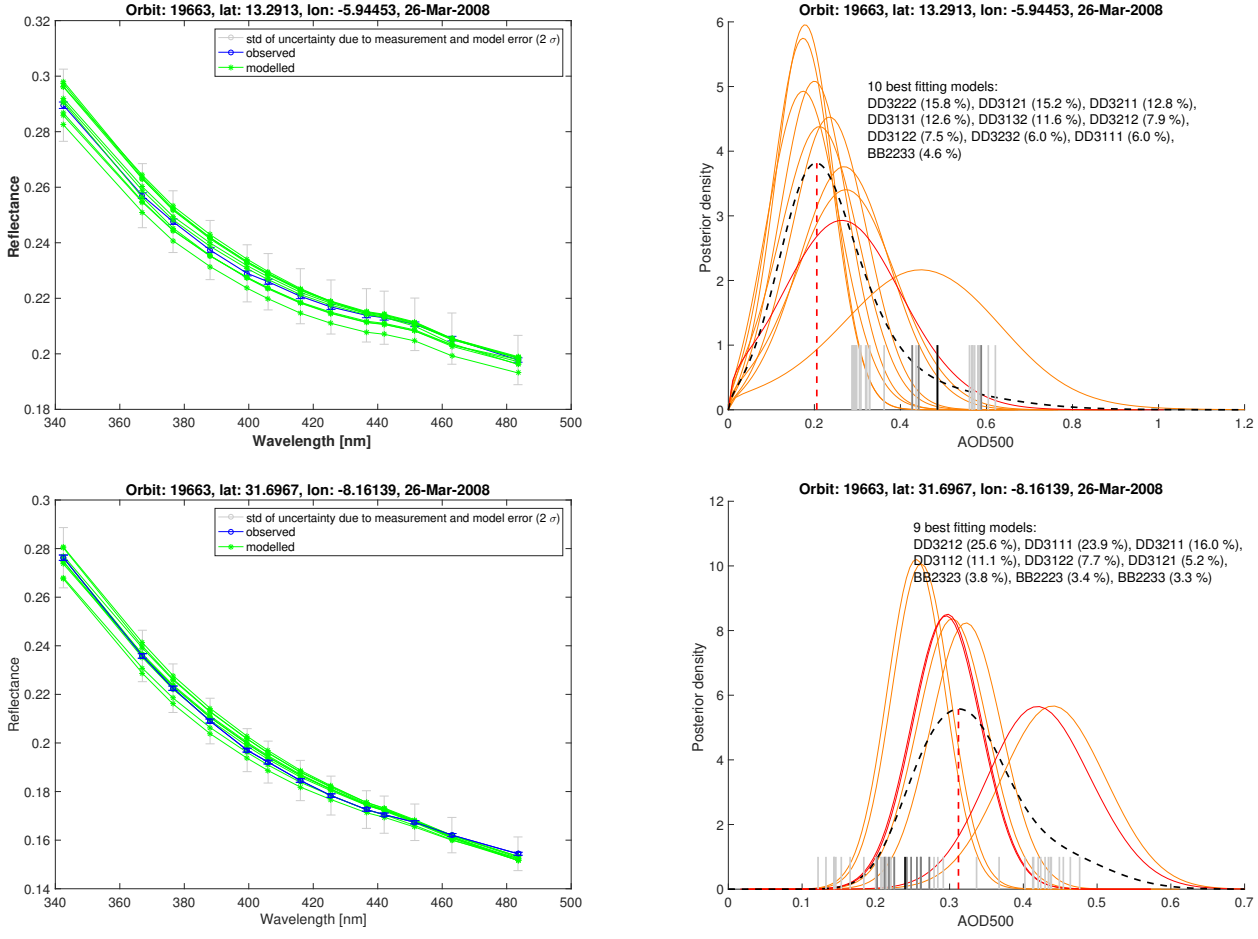

Figure 16. Same as Fig. 15 but for the pixels located at IER_Cinzana (upper row) and Saada (lower row). Right column: The desert dust type models' posterior density curves are marked with orange colour and biomass burning type models' with red.

Atmos. Meas. Tech. Discuss., doi:10.5194/amt-2017-47, 2017
Manuscript under review for journal Atmos. Meas. Tech.
Discussion started: 22 March 2017

Atmospheric Measurement Techniques Discussions

Table 1. Aerosol size distribution parameters and wavelength dependent single scattering albedo (SSA) for aerosol microphysical models stored in LUTs. The third digit ('x') in the model ID number for BB and DD models has a range of 1–3 and is intended for different vertical distributions. The size distribution is given by log-normal functions. The mean particle radius, rg [micron], and the standard deviation, σ [micron], are given for both modes, m1 and m2. A second mode fraction of the number concentration is given in column 'n21'. The SSA depend on wavelength and the values shown here are for the first and last wavelength band.

Model	rg m1	rg m2	σ m1	σ m2	n21	SSA
WA1111	0.078	0.497	1.499	2.160	4.36e-4	1–1
WA1112	0.088	0.509	1.499	2.160	4.04e-4	1–1
WA1113	0.137	0.567	1.499	2.160	8.10e-4	1–1
WA1114	0.030	0.240	2.030	2.030	1.53e-2	1–1
WA1211	0.078	0.497	1.499	2.160	4.36e-4	0.96–0.95
WA1212	0.088	0.509	1.499	2.160	4.04e-4	0.97–0.96
WA1213	0.137	0.567	1.499	2.160	8.10e-4	0.97–0.98
WA1311	0.078	0.497	1.499	2.160	4.36e-4	0.91–0.88
WA1312	0.088	0.509	1.499	2.160	4.04e-4	0.91–0.90
WA1313	0.137	0.567	1.499	2.160	8.10e-4	0.92–0.92
BB21x1	0.074	0.511	1.537	2.203	1.70e-4	0.94–0.93
BB21x2	0.087	0.567	1.537	2.203	2.06e-4	0.94–0.93
BB21x3	0.124	0.719	1.537	2.203	2.94e-4	0.93–0.94
BB22x1	0.074	0.511	1.537	2.203	1.70e-4	0.90–0.88
BB22x2	0.087	0.567	1.537	2.203	2.06e-4	0.90–0.89
BB22x3	0.124	0.719	1.537	2.203	2.94e-4	0.89–0.90
BB23x1	0.074	0.511	1.537	2.203	1.70e-4	0.86–0.82
BB23x2	0.087	0.567	1.537	2.203	2.06e-4	0.86–0.84
BB23x3	0.124	0.719	1.537	2.203	2.94e-4	0.84–0.85
DD31x1	0.042	0.670	1.697	1.806	4.35e-3	0.82–0.94
DD31x2	0.052	0.670	1.697	1.806	4.35e-3	0.86–0.95
DD32x1	0.042	0.670	1.697	1.806	4.35e-3	0.74–0.90
DD32x2	0.052	0.670	1.697	1.806	4.35e-3	0.79–0.91
VO4111	0.230	0.230	0.800	0.800	0.5	1–1

Atmos. Meas. Tech. Discuss., doi:10.5194/amt-2017-47, 2017
Manuscript under review for journal Atmos. Meas. Tech.
Discussion started: 22 March 2017

Atmospheric Measurement Techniques Discussions

Table 2. The retrieved aerosol characteristics for AERONET sites and results from the presented method. The collocated OMI pixel indices in orbit are given in the column 'Pixel ind'. The AERONET AOD at 440 and the Ångström exponent α(440-675) nm are daily averages of the data from Level 2.0 Version 2 Direct sun algorithm. We interpolated AERONET AOD at 500 nm (marked by *) by Ångström power law using the instant values of α(440-675) nm and AOD at 440 nm. The AOD at 500 nm retrieved by the presented method is the MAP estimate of the averaged posterior density. The Ångström exponents α1(442-500) nm and α2(442-500) nm are calculated from the best matching model LUT and from the second best matching model LUT, respectively. We interpolated OMAERO AOD at 500 nm (marked by **) in the best fitting LUT using AOD at 342.5 nm.

Site Name AERONET	(Lat, Lon) AERONET	Pixel ind OMI	AOD 440 AERONET	AOD 500 AERONET	α(440-675) AERONET	AOD 500	α1	α2	AOD 500 OMAERO
Beijing [a)]	(39.9° N, 116.3° W)	(1029,25)	2.488	2.160*	1.108	3.602	1.008	1.610	-
Beijing [b)]	(39.9° N, 116.3° W)	(1004,12)	0.807	0.665*	1.522	0.624	1.560	1.259	-
Agoufou	(15.3° N, 1.4° W)	(905,9)	0.228	0.218*	0.375	2.549	0.293	-	1.557**
DMN_Maine_Soroa	(13.2° N, 12.0° E)	(873,53)	0.143	0.139*	0.267	0.087	0.978	1.560	0.148**
IER_Cinzana	(13.2° N, 5.9° W)	(899,2)	0.424	0.414*	0.236	0.206	0.561	0.290	0.234**
Saada	(31.6° N, 8.1° W)	(1047,6)	0.302	0.276*	0.697	0.312	0.561	0.290	-

[a)] 16.4.2008 [b)] 27.4.2008